Res Chem Intermed (2017) 43:3463–3471
DOI 10.1007/s11164-016-2427-9

Near-infrared quantum cutting in Tb^{3+} and Yb^{3+}-doped Y_2O_3 nanophosphors

Abhijit P. Jadhav[1] · Sovann Khan[1,2] · Sun Jin Kim[1] · Seung Yong Lee[1,2] · Jong-Ku Park[1] · So-Hye Cho[1,2]

Received: 12 November 2014 / Accepted: 14 January 2015 / Published online: 21 January 2016

Abstract Properties of the quantum-cutting phosphors are dependent on various factors such as dopant concentration, crystallinity, homogeneity, particle size and surface morphology. Effective control of the above parameters can enhance the quantum-cutting ability of the phosphor material. Nano-sized particles of Y_2O_3:-Tb^{3+},Yb^{3+} were prepared with a solution-based co-precipitation method and subsequent calcination. Effective control of the reaction parameters and doping concentration helped to produce uniform nanostructures with high quantum-cutting efficiency up to 181.1 %. The energy transfer mechanism between Tb^{3+} and Yb^{3+} was studied by considering their spectroscopic properties and time-resolved spectroscopy. The high efficiency and small particle size of the quantum-cutting phosphor Y_2O_3:Tb^{3+},Yb^{3+} make it a suitable candidate for its application in solar cells.

Keywords Yttrium oxide · Co-precipitation · Quantum cutting · Nanoparticles · Phosphors

Introduction

Witnessing significant development of the photovoltaic (PV) industry over the past few decades, researchers are still struggling for an efficient and cost-effective conversion of solar energy into electricity through PV cells. Quantum cutting through down-conversion is able to split one incident photon into two (or more) lower-energy

✉ So-Hye Cho
sohyec@kist.re.kr

[1] Materials Architecturing Research Center, Korea Institute of Science and Technology, Hwarangno 14-gil 5, Seongbuk-gu, Seoul 02792, Republic of Korea

[2] Department of Nanomaterial Science and Engineering, Korea University of Science and Technology, Gajeong-ro 217, Yuseong-gu, Daejon 04763, Republic of Korea

photons with conversion efficiency exceeding 100 % [1]. With incorporation of quantum-cutting phosphors, the loss of energy caused due to thermalization of hot charge carriers after the absorption of the high-energy photons can be avoided by the absorption of high-energy photons by the solar cell through down-conversion phosphors. Trupke et al. [2] showed that incorporation of quantum-cutting phosphors in solar cells can effectively enhance its conversion efficiency by up to 38.6 %.

Solar cells are typically composed of special light-absorbing semiconducting materials. Incorporation of wavelength-converting phosphors in solar cell assemblies for up- and down-conversion of the solar spectrum is in large demand. Since quantum-cutting phosphors have ability to split one incident high-energy photon into two (or more) lower-energy photons with a conversion efficiency higher than 100 %, applying quantum-cutting phosphors that show emission near the band gap of a solar cell can significantly improve the cell efficiency over the Shockley–Queisser limits. When applied to a solar cell, those quantum-cutting materials are supposed to be placed on top of the solar cell (facing the Sun) so that the high-energy photons (wavelength < 400 nm) can be converted into lower-energy photons [visible or near-infrared (NIR) light] before they reach the solar cell. Therefore, the ideal design for quantum-cutting phosphors in solar cell is their incorporation in a thin transparent layer on top of the solar cell. To realize the transparent layer, the size of quantum-cutting phosphors needs to be controlled, with dimensions smaller than ~ 150 nm to avoid light scattering [3]. There have been several research papers published for the development of quantum-cutting phosphors for solar cells but only a few considered their size aspects [4, 5].

In this work, we focus on the synthesis of nano-sized, quantum-cutting phosphors with a higher energy transfer rate and external quantum efficiency. Their properties are dependent on various factors such as dopant concentration, crystallinity, homogeneity, particle size and surface morphology. Effective control of the above parameters can enhance the quantum-cutting ability of the phosphor material. The high quantum-cutting efficiency of the down-converting $Y_2O_3:Tb^{3+},Yb^{3+}$ nanophosphors makes it a suitable candidate for a transparent layer of solar cells.

Experimental

Materials

Yttrium (III) chloride hexahydrate ($YCl_3 \cdot 6H_2O$, Chemical Pure, Daejung Chemicals, Korea), terbium (III) chloride ($TbCl_3$, 99.9 %, Sigma-Aldrich, MO, USA), ytterbium (III) chloride hexahydrate ($YbCl_3 \cdot 6H_2O$, 99.9 %, Sigma-Aldrich, MO, USA), oleic acid ($C_{18}H_{34}O_2$, Daejung Chemicals, Korea), sodium chloride (NaCl, Junsei Chemicals, Japan) and sodium carbonate hydrate ($Na_2CO_3 \cdot H_2O$, extra pure, Daejung Chemicals, Korea) were used as received without further purification.

Synthesis

The synthesis of Yb- and Tb-doped yttrium oxide was carried out using a co-precipitation method reported previously [6]. Powder samples of Y_2O_3 were prepared

by the stoichiometric ratio of $Y_{1.9-x}O_3{:}Tb_{0.1}Yb_{x\ \%}$ ($x = 0$–0.2). The precursors were weighed carefully in respective reaction flasks and dissolved in 50 mL of aqueous solution. Oleic acid (1.0 mL, 3.2 mmol) was added to the aqueous solution and NaCl was added to make a 0.15 M-concentration. The emulsion was stirred at room temperature for 1 h and then the pH of the solution was adjusted to 7.0 by the dropwise addition of sodium carbonate aqueous solution ($Na_2CO_3{\cdot}H_2O$, 0.3 M). A white-colored precipitate formed after addition of the sodium carbonate, indicating the formation of carbonate complexes, as indicated in the Eq. 1.

$$2YCl_3 \cdot 6H_2O + 2TbCl_3 + 2YbCl_3 \cdot 6H_2O + 9Na_2CO_3 \xrightarrow[H_2O]{\text{oleic acid}} (Y, Tb, Yb)_2(CO_3)_3 \cdot 12H_2O + 18NaCl + 6CO_2 + 12H_2O + 3O_2 \quad (1)$$

The stirring was continued for 2 h at room temperature and the precipitate was then separated by centrifugation at 10,000 rpm for 10 min. The obtained solid was washed thoroughly using deionized (DI) water for 3 times and then washed with ethanol twice to remove organic impurities, resulting in a white solid. The solid was dried in an oven at 120 °C for 4 h and calcinated at 800 °C for 2 h under an ambient condition. The carbonate complexes turned to oxide complexes by sequential decarboxylation during the calcination, as indicated in the Eq. 2.

$$(Y, Tb, Yb)_2(CO_3)_3 \cdot 12H_2O \xrightarrow[-12H_2O]{} (Y, Tb, Yb)_2(CO_3)_3 \xrightarrow[-2CO_2]{} (Y, Tb, Yb)_2O_2(CO_3) \longrightarrow (Y, Tb, Yb)_2O_3 \cdot CO_2 \xrightarrow[-CO_2]{} Y_2O_3{:}Tb^{3+}Yb^{3+} \quad (2)$$

Characterizations

The powder X-ray diffraction (XRD) patterns of the annealed samples were recorded using CuKα radiation ($\lambda = 1.54056$ Å) on a Bruker D8 Advanced diffractometer operating at 40 kV and 40 mA at a scanning rate of 05° per step in the 2θ range of $10° \leq 2\theta \leq 120°$. The reference data for the comparison of obtained diffraction patterns were obtained from JCPDS cards. Particle size and morphology of the calcinated nanophosphors were detected by field emission scanning electron microscopy (FE-SEM, model FEI-XL30 FEG [field emission gun], accelerating voltage = 15 kV; FEI Co., Hillsboro, OR, USA) and transmittance electron microscopy (TEM, model Tecnai G2, accelerating voltage = 200 kV; FEI Co., Hillsboro, OR, USA). The photoluminescence spectroscopy of the quantum-cutting phosphor was measured by a Hitachi F-7000 fluorescence spectrophotometer with a 200-W xenon lamp source (Hitachi, Japan).

Results and discussion

As represented in Fig. 1, the crystalline Y_2O_3 has a cubic bixbyite structure with an *Ia*3 space group, containing 16 formula units in each primitive cell [7]. Among the 32 six-fold coordinated cations in its primitive cell, 8 are centrosymmetric with C_{3i}

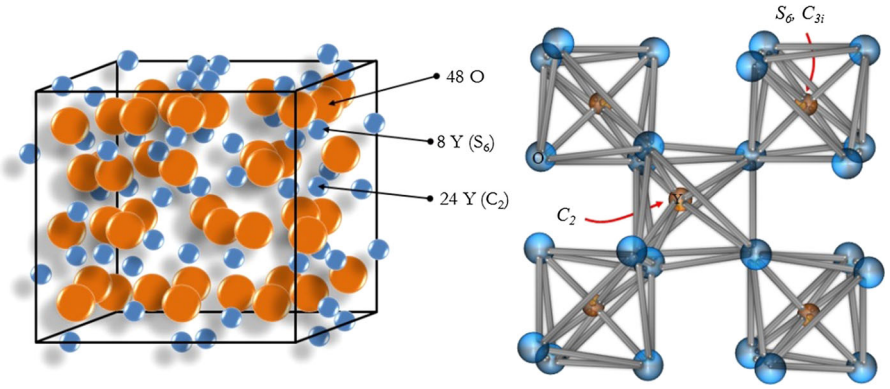

Fig. 1 Cubic bixbyite structure of Y_2O_3 with C_2 and C_{3i}/S_6 symmetry sites

symmetry, and 24 are non-centrosymmetric with C_2 symmetry. While the point symmetries of S_6 and C_{3i} have an inversion center and smaller crystal field, disallowing electron–dipole transitions in the absence of lattice distortion (thermal or due to impurity incorporation), the C_2 sites are non-centrosymmetric, i.e. have no center of inversion allowing electron–dipole transitions and, therefore, being predominantly responsible for the luminescent emissions when occupied by transition metal ions [8]. The cubic phase of yttrium oxide shows the presence of Y^{3+} in two different environments (C_2 or S_6) with six oxygen atoms surrounding it. The isomorphic substitution of terbium and ytterbium ions in a Y_2O_3 lattice will usually occupy these symmetry sites (low-symmetry C_2 and high-symmetry S_6). As the number of C_2 sites is about three times higher than number of S_6 sites, the dopant ions Tb and Yb occupy more C_2 positions than S_6 positions.

Figure 2 represents XRD patterns of Y_2O_3 phosphors with various concentrations of Yb (0–10 mol%) with a fixed amount of Tb (5 mol%). All of the Bragg reflections in the diffraction patterns were indexed by comparing with standard diffraction peaks of the body-centered cubic structure (space group I_{a3}) of Y_2O_3 (JCPDS # 83-0927). No additional secondary phase, impurities or any traces of amorphous nature were observed, indicating the structural purity of the synthesized compounds. This result also indicates that high lanthanide doping levels up to 15 mol% in respect to Y^{3+} can be used in Y_2O_3 crystal without altering the basic structure of the host under the synthesis conditions. The respective changes in lattice parameters and unit cell volume due to increasing amount of dopants are summarized in Table 1. Doping with 5-mol% terbium ions, the unit cell volume increased by 13.04 $Å^3$ in respect with the standard Y_2O_3 sample. With increasing dopant concentration of ytterbium ions to $Y_{1.9}O_3$:$Tb_{0.1}$, the unit cell volume showed minimal deviation from that of the $Y_{1.9}O_3$:$Tb_{0.1}$ sample. Those changes in the unit cell volume are affected by the differences in the ionic radii of the Y^{3+}, Tb^{3+} and Yb^{3+} ions [$r(Y^{3+}) = 1.019$ Å, $r(Tb^{3+}) = 1.040$ Å and $r(Yb^{3+}) = 0.985$ Å; for the coordination number (CN) 8] [9].

The size and morphology of the Y_2O_3 phosphors were analyzed by SEM and TEM images. Figure 3 shows SEM images of $Y_{1.9-x}O_3$:$Tb_{0.1}$,Yb_x ($x = 0$, 0.02, 0.06, 0.10, 0.14, and 0.20) in series. When the doping concentration of ytterbium ion was below

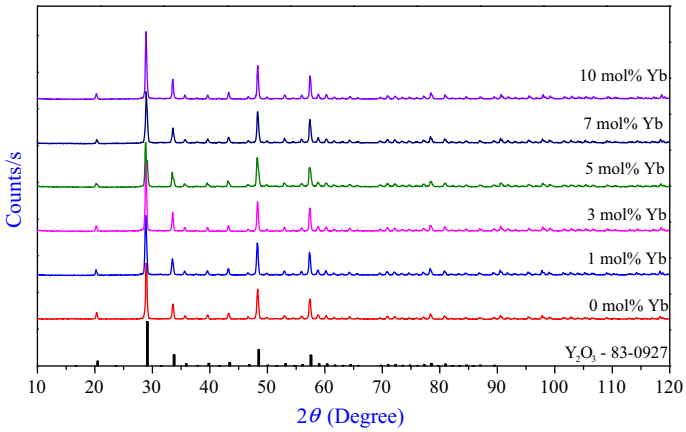

Fig. 2 Comparison of XRD patterns of $Y_{1.9-x}O_3$:$Tb_{0.1}$,Yb_x ($x = 0, 0.02, 0.06, 0.10, 0.14, 0.20$) prepared by a co-precipitation method and calcined at 800 °C for 2 h

Table 1 Unit cell parameters for $Y_{1.9-x}O_3$:$Tb_{0.1}$,Yb_x calcinated at 800 °C for 2 h in air

Sample	a (Å)	Deviation in a (Å) from the std.	Cell volume (Å^3)	Deviation in cell volume from the std. (Å^3)
JCPDS (83-0927)	10.608	–	1193.70	–
$Y_{1.9}O_3$:$Tb_{0.1}$	10.6464	+0.0384	1206.74	+13.04
$Y_{1.88}O_3$:$Tb_{0.1}$,$Yb_{0.02}$	10.6609	+0.0529	1211.67	+17.97
$Y_{1.84}O_3$:$Tb_{0.1}$,$Yb_{0.06}$	10.6494	+0.0414	1207.74	+14.04
$Y_{1.8}O_3$:$Tb_{0.1}$,$Yb_{0.1}$	10.6596	+0.0516	1211.23	+17.53
$Y_{1.76}O_3$:$Tb_{0.1}$,$Yb_{0.14}$	10.6468	+0.0388	1206.86	+13.16
$Y_{1.7}O_3$:$Tb_{0.1}$,$Yb_{0.2}$	10.6466	+0.0386	1206.80	+13.10

3 mol%, the particle size was below 40 nm and the particle morphology was more or less spherical and homogeneous. However, when the doping levels were increased more than 5 mol%, the grain size grew bigger, reaching 60–70 nm with 10-mol% Yb doping. The particle morphology also changed to rough and irregular and agglomeration was found in some portion. To study the microstructure and crystallinity of the Y_2O_3 phosphors, a TEM image of $Y_{1.84}O_3$:$Tb_{0.1}$,$Yb_{0.06}$ phosphor was examined and shown in Fig. 4. The particle morphology was more or less spherical with a little facet on the surface, and the crystallinity appeared to be very high.

The spectroscopic properties of the Y_2O_3 phosphors were examined with photoluminescence spectroscopy and the results are shown in Figs. 5 and 6. Under the excitation of UV light ($\lambda_{exc.} = 304$ nm), both visible light emission within 470–700 nm and NIR light emission within 950–1050 nm were observed. Several lines in the visible range correspond to the multiplet electronic transition of $^5D_4$–^7F_J ($J = 6, 5, 4, 3, 2$) of Tb^{3+}, whereas the NIR light emission corresponds to electronic transition between Stark levels of $^2F_{5/2}$ and $^2F_{7/2}$ of Yb^{3+}. The luminescence excitation spectrum through emission at 545 nm showed broad absorption in the

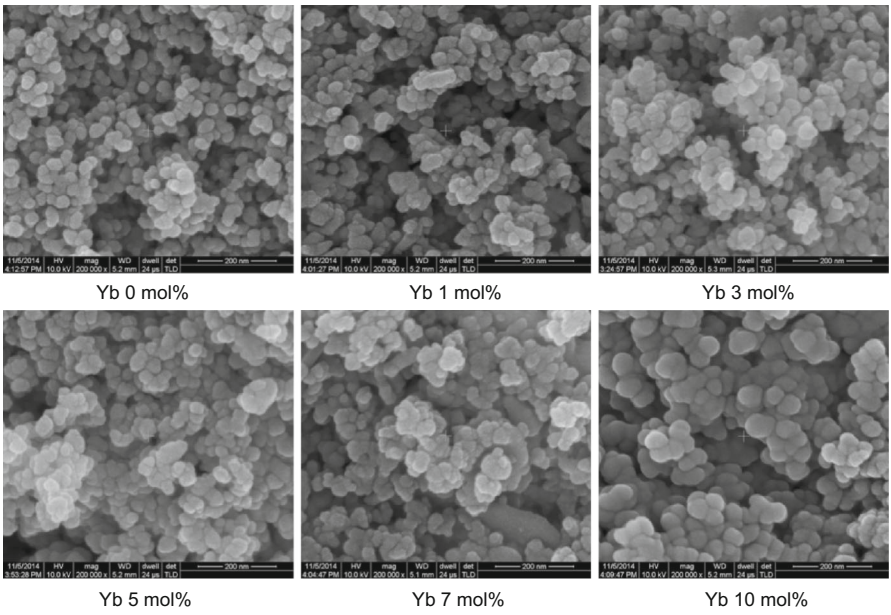

Fig. 3 Comparison of SEM images of $Y_{1.9-x}O_3{:}Tb_{0.1},Yb_x$ ($x = 0$, 0.02, 0.06, 0.10, 0.14, and 0.20) by the doping concentration of ytterbium ions

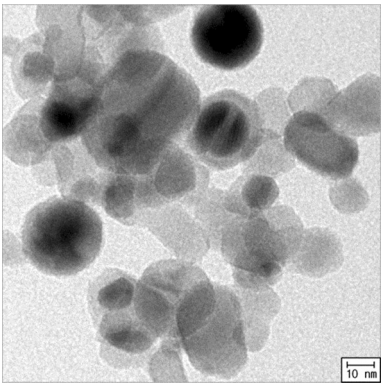

Fig. 4 TEM image of $Y_{1.84}O_3{:}Tb_{0.1},Yb_{0.06}$ nanophosphor

range of 200–330 nm. Van Pieterson et al. [10] explained that the charge transfer absorption of O^{2-}–Yb^{3+} in yttrium oxide is found in the region of $\lambda < 250$ nm; thus, it is clear that the observed absorption band relates to electronic transition of $Tb^{3+}(^7F_6) \rightarrow Tb^{3+}(4f^75d^1)$. As the Yb^{3+} concentration was increased from 0 to 10 mol%, the visible light emission decreased gradually, as shown in Fig. 5; whereas, the NIR emission was increased along with Yb^{3+} concentration, as indicated in Fig. 6. The NIR emission of Yb^{3+} originates from the energy transfer of Tb^{3+} to Yb^{3+} since the intra-ion relaxation rate of $Tb^{3+}(^5D_4) \rightarrow Tb^{3+}(^7F_J)$ is relatively slower than the inter-ion transition of $Tb^{3+}(^5D_4) \rightarrow 2Yb^{3+}$ ($^2F_{5/2}$). With

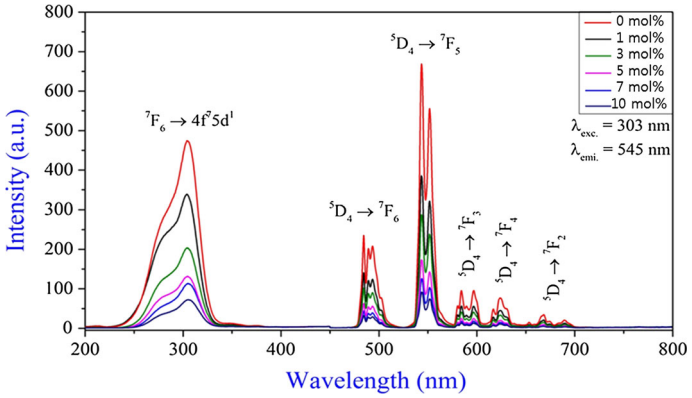

Fig. 5 Excitation and emission spectra of $Y_{1.9-x}O_3$:$Tb_{0.1}$,Yb_x ($x = 0$, 0.02, 0.06, 0.10, 0.14, and 0.20)

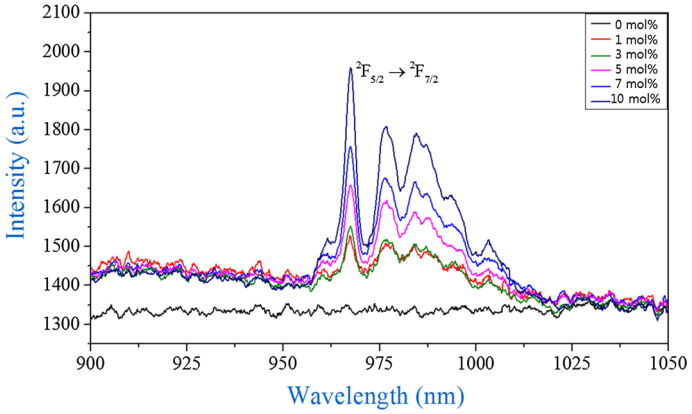

Fig. 6 NIR emission spectra of $Y_{1.9-x}O_3$:$Tb_{0.1}$,Yb_x ($x = 0$, 0.02, 0.06, 0.10, 0.14, and 0.20)

absorption of UV light, Tb^{3+} ions are excited up to its $4f^75d^1$ energy level and successively follow fast intra-ion relaxation to a $^5D_4$ level, denoted as a green line in Fig. 7. The relaxed photon at $^5D_4$ gives spontaneous $^5D_4$–^7F_J ($J = 0$–6) emission and cooperative energy transfer between $Tb^{3+}(^5D_4) \rightarrow 2Yb^{3+}(^2F_{5/2})$ with some degree of deactivation by quenching, denoted as red and dotted lines, respectively, in Fig. 7 [11]. In an effective doping system, a single cooperative acceptor of the Yb–Yb type is formed where two Yb^{3+} ions occupy the nearest neighboring coordination sphere of Tb^{3+} [12].

NIR quantum cutting for Tb^{3+}–Yb^{3+} co-doped systems was first studied and reported by Vergeer et al. [11] on YPO_4 phosphors. They proposed a cooperative quantum-cutting mechanism by analyzing the time-resolved spectroscopic study of Tb^{3+} as a function of Yb^{3+} doping concentration. For the Tb^{3+}–Yb^{3+} couple, the transition of Tb^{3+} ($^5D_4 \rightarrow {}^7F_J$) is approximately twice the energy of $^2F_{5/2} \rightarrow {}^2F_{7/2}$ transition of Yb^{3+}. The energy transfer and quantum efficiencies were calculated from the luminescence decay curves using the following equations,

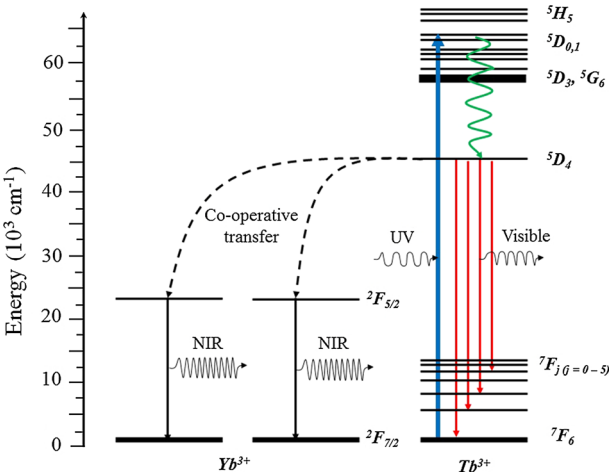

Fig. 7 Quantum cutting through cooperative energy transfer between $Tb^{3+} \rightarrow Yb^{3+}$

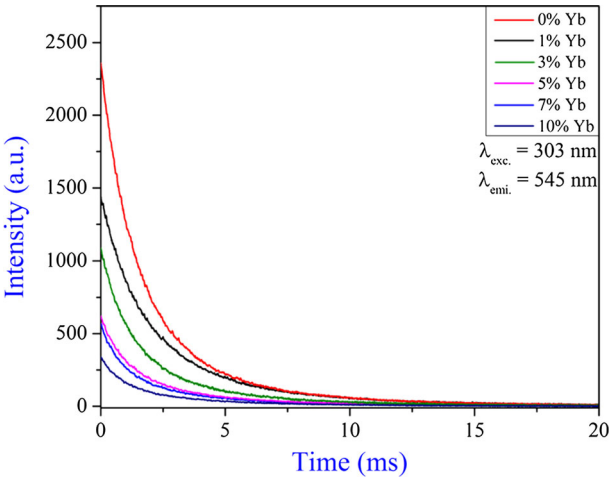

Fig. 8 Time-resolved luminescence spectroscopy of Tb^{3+} $^5D_4$–$^7F_5$ emission at 545 nm for various concentrations of Yb^{3+} under an excitation of 303 nm

$$\eta_{ET} = \eta_{x\%Yb} = 1 - \frac{\int I_{x\%Yb}dt}{\int I_{0\%Yb}dt} \tag{3}$$

$$\eta_{QE} = \eta_{Tb}(1 - \eta_{ET}) + 2\eta_{ET} \tag{4}$$

where I denotes intensity, x %Yb stands for Yb concentration and η_{Tb} represents quantum efficiency (QE) for Tb^{3+} and is set to 1 [11].

Following the calculation method suggested by Vergeer et al., quantum efficiencies of our Y_2O_3 phosphors were obtained from the respective decay time

of Tb^{3+}: 2.28, 1.86, 1.84, 1.82, 1.80 and 1.74 ms for samples prepared with 0, 1, 3, 5, 7 and 10 mol% of Yb^{3+}, respectively (Fig. 8). By taking the upper limited value of the cooperative energy transfer efficiency as assuming the $Tb^{3+}(^5D_4) \rightarrow 2Yb^{3+}$ ($^2F_{5/2}$) cooperative transfer is 100 %, the theoretical quantum efficiency is calculated to be 67.3, 139.1, 164.5, 169.5, and 181.1 % for samples prepared with 1, 3, 5, 7 and 10 mol% of Yb^{3+}, respectively. However, there is a limitation to providing further insight on the QE results because there is much assumption applied in their calculation. On the other hand, the measurement of internal and external QEs was difficult as photon detectors used for visible and NIR regions were different.

Conclusion

Rare-earth-doped Y_2O_3 nanocrystals were synthesized by a co-precipitation method and subsequent calcination at 800 °C. The nanocrystals were found to be uniform in size and highly crystalline with an average diameter of $\sim$50 nm. With Tb^{3+} and Yb^{3+} co-doped Y_2O_3, the energy transfer mechanisms in the visible and NIR region were studied by considering their photoluminescence spectrums and time-resolved luminescence techniques. Photons excited by UV to a Tb^{3+} $4f^75d^1$ energy level and subsequently relaxed to a $^5D_4$ level appear to transfer to Yb^{3+} $^2F_{5/2}$ level, resulting in NIR emission. Quantum efficiencies of $Y_{1.9-x}O_3$:$Tb_{0.1}$,Yb_x were calculated following the method suggested by Vergeer et al. [11] and a QE as high as 181.1 % was obtained with 10-mol% Yb doping. Since these $Y_{1.9-x}O_3$:$Tb_{0.1}$,Yb_x phosphors were designed to be nano-sized in order to avoid light scattering, they can make good candidates for applications in solar cell devices. Efforts to make them into a transparent layer for silicon solar cell panels are in progress.

Acknowledgments We thank the financial support from the Korea Institute of Science and Technology (KIST) institutional funding (Project No. 2E26120) and the international cooperation program managed by the National Research Foundation of Korea (NRF-2014K1A3A1A09063246).

References

1. Q.Y. Zhang, X.Y. Huang, Prog. Mater. Sci. **55**, 353 (2010)
2. T. Trupke, M.A. Green, P. Wurfel, J. Appl. Phys. **92**, 1668 (2002)
3. W.G.J.H.M. van Sark, A. Meijerink, R.E.I. Schropp in *Solar Spectrum Conversion for Photovoltaics Using Nanoparticles, Third Generation Photovoltaics*, ed. by V. Fthenakis (In Tech, 2012), p. 1
4. H. Lin, D.Q. Chen, Y.L. Yu, A.P. Yang, Y.S. Wang, Opt. Lett. **36**, 876 (2011)
5. Q.Y. Zhang, C.H. Yang, Z.H. Jiang, X.H. Ji, Appl. Phys. Lett. **90**, 061914 (2007)
6. A.P. Jadhav, A. Pawar, C.W. Kim, H.G. Cha, U. Pal, Y.S. Kang, J. Phys. Chem. C **113**, 16652 (2009)
7. F. Hanic, M. Hartmanova, G.G. Knab, A.A. Urusovskaya, K.S. Bagdasarov, Acta Crystallogr. B **40**, 76 (1984)
8. M. Klintenberg, S. Edvardsson, J.O. Thomas, J. Alloys Compd. **275**, 174 (1998)
9. P. Ayyub, V.R. Palkar, S. Chattopadhyay, M. Multani, Phys. Rev. B **51**, 6135 (1995)
10. L. van Pieterson, M. Heeroma, E.D. Heer, A. Meijerink, J. Lumin. **91**, 177 (2000)
11. P. Vergeer, T.J.H. Vlugt, M.H.F. Kox, M.I. den Hertog, J.P.J.M. van der Eerden, A. Meijerink, Phys. Rev. B **71**, 014119 (2005)
12. J.L. Yuan, X.Y. Zeng, J.T. Zhao, Z.J. Zhang, H.H. Chen, X.X. Yang, J. Phys. D Appl. Phys. **41**, 105406 (2008)